How gable roofs change the mechanisms of vertical momentum transfer: a LES study on two-dimensional urban canyons

Maria Grazia Badas[1], Michela Garau[1], Giorgio Querzoli[1]

Received: DD Month YEAR/ Accepted: DD Month YEAR

Abstract. A Large Eddy Simulation (LES) study on the presence of gable roofs in urban canyons is presented: two canyon aspect ratios, $AR_C = 1, 2$, ($AR_C = W/H$ corresponding to the ratio of the canyon width, W, to the eaves' height, H) and variable roof slope, α ($\alpha = 0°, 10°, 20°, 30°, 45°$) in a periodic configuration are considered. The vertical turbulent momentum flux is analysed by means of the quadrant analysis both in terms of spatial maps and mean vertical profiles in order to assess how the presence of a gable roof and its slope affects the mechanisms of mixing in the roughness sublayer. A gradual modification with increasing roof slope is apparent for the mean flow patterns as well as for the shear layer thickness. On the contrary, the contribution of ejections and sweeps at the rooftop goes through an abrupt change when passing from flat- to gable-roof buildings. This behaviour arises for both the investigated flow regimes. We observed that with gable roofs the imbalance between sweeps and ejections is monotonically increasing with α. However, the case of flat roof is not in continuity with the small pitch ones, as it gives much higher values of imbalance, comparable to what was observed for the largest analysed pitches (45°).

Keywords Street canyon · Urban boundary layer · Gable roof · Large Eddy Simulation · Quadrant analysis

✉ Maria Grazia Badas
mgbadas@unica.it

[1] DICAAR, Università degli Studi di Cagliari, Cagliari, Italy

1 Introduction

Shaping the urban environment is a crucial issue in order to control the breathability of the cities where the pollutant concentration levels suggested by the World Health Organization are often exceeded (WHO 2006; Air Quality in Europe 2018). Studies on realistic geometries are useful to address specific site studies, but they are unfeasible to infer general conclusions or to understand physical phenomena. As a consequence, research in this field often relies on schematic and idealized simulations (Zajic et al., 2015, 2011; Di Bernardino et al., 2020). In this perspective, the street canyon unit represents a simple, yet effective, scheme to get insight on the basic phenomena and to single out the effect of some specific urban elements. Moreover, investigations on urban canyons allow the development of simple parameterizations needed in mesoscale models, which rely on the synthetic representation of the canyon unit (Martilli et al., 2002).

The simplest urban canyon configuration is represented by a two-dimensional periodic scheme, which received much attention in literature, both in laboratory and numerical works. Many issues have been investigated on this simple unit, from the onset of different flow regimes according to the canyon aspect ratio (Oke, 1988), and its effect on turbulent kinetic energy budget (Di Bernardino et al., 2015a; Di Bernardino et al., 2015b), to the influence of the building aspect ratio (Badas et al., 2020), the role of the small-scale roughness placed on the top of the buildings (Salizzoni et al., 2008), the mechanism of pollutant removal from the canyon (Chung and Liu, 2013; Liu et al., 2011; Liu and Wong, 2014), the role of buoyancy (Cai, 2012; Cheng and Liu, 2011a) and many others.

Roofs represent a common feature in buildings, and investigations on their effect in urban context have recently received much attention in literature. For instance, Tominaga et al. (2015) worked on the influence of roof pitches on the air flow in case of isolated buildings, while Shao et al. (2019) analysed the characteristics of cladding and structural loads for hip-roofed buildings, Chen et al. (2019) studied the effects on wind loads of gable-roof buildings with different roof slopes, Xing et al. (2018) demonstrated how roof pitches affect the pressure distributions around isolated buildings and Gullbrekken et al. (2018) experimentally measured wind pressure coefficients aimed at evaluating the roof ventilation. Indeed, the role of the roof is central also in street canyon flows: in his pioneering work Rafailidis (1997) found out that the roof shape highly alters the flow dynamics, potentially beneficing the urban air quality. This statement was confirmed by other authors who investigated the presence of roofs in urban canyons, with both numerical and experimental techniques (Badas et al., 2017; Ferrari et al., 2017; Huang et al., 2015; Takano and Moonen, 2013; Yassin, 2011), proving how roof slope is crucial in modifying turbulence levels at the interface between the canyon and the overlaying airflow, and may produce relevant impacts on natural ventilation compared to the flat roof buildings. Llaguno-Munitxa et al. (2017) remarked the roof positive role on the turbulence and mixing above a building array, while emphasizing the negative role of façade elements such as balconies. Despite these efforts, a parametric study on how the gable roof pitch affects the momentum transfer between the canyon and the above boundary layer is missing in literature. Here, Large Eddy Simulations (LES) on periodic urban canyons are performed with this aim, focusing the analysis on two canyon aspect ratios ($AR_C = W/H = 1, 2$) that are characteristic of urban texture. The present investigation is mainly carried out by means of the so-called quadrant analysis (QA), a simple yet powerful method among the conditional sampling techniques, dating back to the '70s (Wallace et al., 1972), but still widely used to infer important information on the flow.

The paper is organized as follows: the numerical set-up and validation with flume experimental data are presented in Section 2. In Section 3, after a brief introduction of quadrant analysis (QA), the main results are described. Discussion is presented in Section 4 and conclusions are drawn in Section 5.

2 Numerical Set-Up and Validation

The experiments were carried out by means of the Large Eddy Simulation (LES) technique with the open-source CFD code OpenFOAM 2.3. Results were validated against water-channel measurements obtained by Garau et al. (2018). The detailed numerical methodology and validation processes are reported below.

2.1 Numerical methods

Assuming neutral conditions, the flow can be described by the continuity and Navier-Stokes equations, which, according to the classical LES scheme, are spatially filtered and can be expressed as:

$$\frac{\partial \bar{u}_i}{\partial x_i} = 0, \tag{1}$$

$$\frac{\partial \bar{u}_i}{\partial t} + \frac{\partial \bar{u}_i}{\partial x_j}\bar{u}_j = -\Delta P \delta_{ij} - \frac{\partial \bar{p}}{\partial x_i} - \frac{\partial \tau_{ij}}{\partial x_j} + \nu \frac{\partial^2 \bar{u}_i}{\partial x_i \partial x_j}, \tag{2}$$

where $\bar{u}_i$ are the resolved-scale velocity components in the i-direction, $\bar{p}$ is the resolved scale kinematic-pressure, ΔP is the kinematic-pressure gradient, δ_{ij} the Kronecker delta and ν is the kinematic viscosity. The sub-grid scale (SGS) Smagorinsky model (Smagorinsky, 1963) was here employed, thus the SGS Reynolds stresses can be written as follow:

$$\tau_{ij} = \left(\overline{u_i u_j} - \bar{u}_i \bar{u}_j\right) = -2\nu_{SGS} S_{ij}, \tag{3}$$

where, ν_{SGS} is the kinematic eddy viscosity, computed as $\nu_{SGS} = C_k \Delta \sqrt{k_{SGS}}$, where $C_k = 0.094$ is an empirical modelling constant, Δ is the filter width ($\Delta = (\Delta_1 \Delta_2 \Delta_3)^{1/3}$), and k_{SGS}, the SGS kinematic energy, is evaluated as:

$$k_{SGS} = \frac{2C_K}{C_\varepsilon} \Delta^2 |S|^2, \tag{4}$$

where C_ε= 0.07. The above equations are solved in OpenFOAM by means of the finite volume method (FVM). Second-order-accurate schemes were adopted for both time and space derivatives. Namely, the backward differencing scheme in the time derivatives, and the central differencing scheme (Gaussian integration with linear interpolation) in the spatial derivatives were applied. The large time-step transient solver for incompressible flow was considered for the pressure-velocity coupling scheme, by means of the PIMPLE algorithm (merged PISO-SIMPLE). The preconditioned conjugate gradient (PCG) method was used to solve the linear equation system for $\bar{p}$ and the preconditioned bi-conjugate gradient (PbiCG) method was chosen for $\bar{u}$. The time-step increment was varied during the simulation in order to assure inside the entire domain Courant numbers, Co, lower than 0.6.

2.2 Computational Domain and Boundary Conditions

The sketch of the computational domain is shown in Fig. 1: three identical street canyons are simulated, with buildings perpendicularly disposed with respect to the wind direction, and two canyon aspect ratios, $AR_C = W/H = 1$ and 2, which correspond respectively to skimming flow and wake interference regimes (Oke, 1988). Buildings are characterised by height of the eaves equal to the width (i.e. $H = W$, see Fig. 1) and by a variable total height, H_{tot}, depending on the roof slope, and ranging from a minimum of $H_{tot} = 1$ with $\alpha = 0°$, up to a maximum of $H_{tot} = 1.5$, with $\alpha = 45°$ (see Fig. 1). In order to match the minimum dimensions requested by most guidelines (Blocken, 2015; Franke et al., 2011; Tominaga et al., 2008) both vertical and span-wise lengths were defined equal to $9H$ (*i.e.* $6\,H_{tot}$ when $\alpha = 45°$), while the stream-wise length is equal to $6H$ when $AR_C = 1$, and to $9H$ when $AR_C = 2$. Periodic boundary conditions were employed for both the stream-wise and span-wise faces of the domain, in order to obtain a periodic regular 2D street canyon arrangement. The number of canyons usually employed on similar configurations is variable (usually ranging from 1 to 5). Actually, Cheng and Liu (2011) demonstrated, by means of the two-point correlation analysis, the good performances achieved by employing three canyons, especially when the mass transport is not simulated. This justifies the choice of the configuration adopted in this work.

The symmetry condition was imposed on the top boundary, while the Spalding wall boundary condition (Spalding, 1962) was assumed both on the ground and on the building walls to model the near-wall flows:

$$y^+ = u^+ + \frac{1}{E}\left[e^{ku^+} - 1 - ku^+ - \frac{1}{2}(ku^+)^2 - \frac{1}{6}(ku^+)^3\right], \qquad (5)$$

where y^+ and u^+ are the non-dimensional wall variables, k is the Von Karman constant and $E(=9)$ is an empirical constant.

In order to set the turbulent initial condition, several inflow turbulence generator techniques (ITGT) can be adopted (Bazdidi-Tehrani et al., 2016). In this work, the instantaneous turbulent velocity fluctuations were superimposed onto the mean velocity field obtained from a precursor RANS (Reynolds Averaged Navier Stokes) simulation, by means of the technique proposed by De Villiers (2006). A transitional time interval, about 35 convective times long ($T_C = L/U_{mean}$, where L is the domain size in stream-wise direction and U_{mean} is the mean velocity) was found necessary to the flow achieve the fully turbulence development. The imposed mean stream-wise velocity allowed obtaining a Reynolds number at the building height, $Re_H = \frac{U_H H}{\nu} = 7000$, which is higher than the minimum needed to obtain the flow independence on Reynolds number which, according to Hoydysh et al., (1974), is $Re_H = 3400$.

We adopted a structured mesh (Fig. 1b), as often done in the case of urban canyons, also in presence of gable roofs (see e.g. Ozmen et al. 2016). The grid is stretched both in the vertical directions and towards the canyon centre with an expansion ratio of 1.2. Consequently, the resolution is equal to $\Delta x = \Delta z = 0.016\,H$ in the proximity of the building walls and the ground, whilst in the canyon center the cell size is doubled. This set up corresponds to 32 cells per building side, higher than the threshold (i.e. 10) prescribed by the guidelines (Tominaga et al., 2008). The resolution in the span-wise direction is equal to $\Delta y = 0.05\,H$. The total number of cells ranges from $7 \cdot 10^6$ (in the case of $AR_C = 1.0$) to $9 \cdot 10^6$ (in the case of $AR_C = 2.0$). As shown in Fig. 1b, the highest cell deformation occurs in case of gable roofs around the corners; nevertheless, the mesh quality was found acceptable as also confirmed by the validation step discussed in section 2.4.

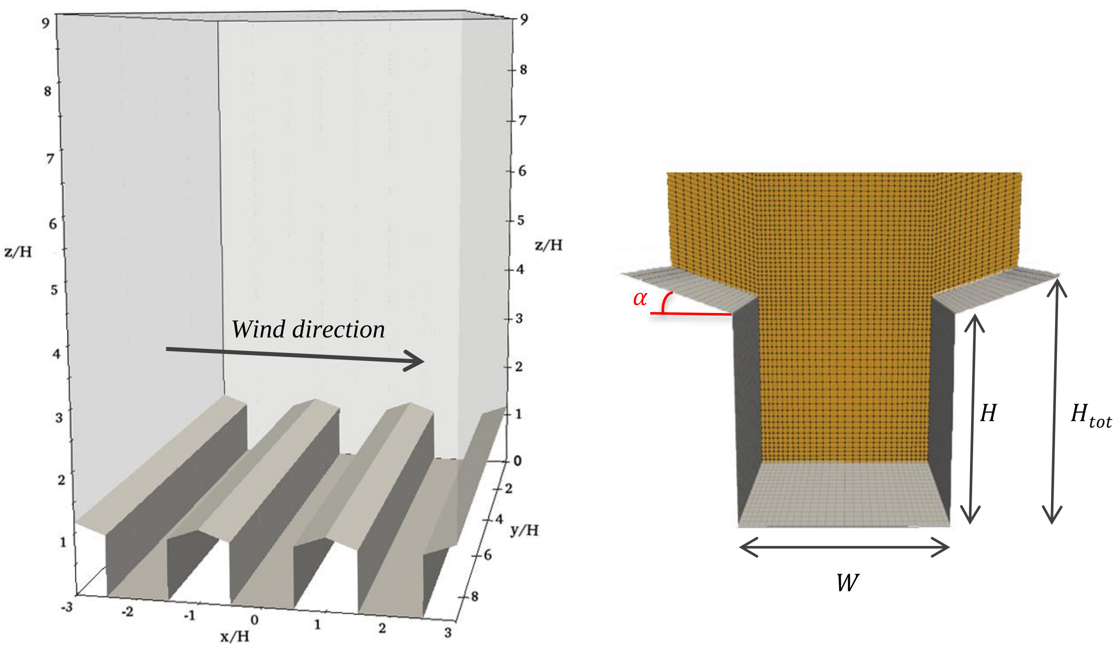

Fig. 1: Left panel: computational domain scheme: $\boldsymbol{H}$ is the eaves height, $\boldsymbol{H_{tot}}$ is the total height of buildings, $\boldsymbol{W}$ is the canyon width, $\boldsymbol{\alpha}$ is the pitch slope and the green region is the canyon unit. Right panel: computational grid.

After the turbulence transition time interval, data were recorded every $0.05T_C$ (where T_c is the convective time), assuring the statistical independence among recorded samples, and simulations were performed for a period of about $70\ T_C$.

2.3 Validation

Statistics were computed by averaging data samples both in time and in space (over the span-wise length), in order to enhance the statistical robustness of dataset, while the analysis was focused only on the central canyon. Model validation was performed by means of the experimental results obtained by Garau et al. (2018). They run experiments above a series of 20 identical prismatic obstacles with square section, variable roof shape (flat, $\alpha = 0°$, and gable roof, $\alpha = 45°$), and canyon aspect ratios, AR_C, ranging from 1 to 6. The experiments were performed in a water flume, where obstacles extended across the entire width of the channel. The velocity measurements were carried out by means of the Feature Tracking Velocimetry (FTV) technique (Besalduch et al., 2014) in the 17th canyon, assuring that the equilibrium of the roughness layer is attained and that the experimental fields are representative of periodic conditions (Llaguno-Munitxa et al., 2017). Four configurations were employed for validation ($AR_C = 1, 2$ both with $\alpha = 0°, 45°$). Fig. 2 displays the profiles of the stream-wise velocity and of the vertical velocity skewness spatially averaged on the canyon periodic unit.

The averaging over the periodic unit (Fig. 1 left panel) is indicated by angle brackets and is computed as:

$$< \bar{\gamma} > (z) = \frac{1}{\lambda(z)} \int_0^b \int_{\lambda(z)} \bar{\gamma}(x, y, z) dx\, dy, \tag{6}$$

where z is the non-dimensional vertical coordinate, b is the spanwise dimension of the domain, the integration variable $\bar{\gamma}$ corresponds to the time average of a generic parameter, γ, and $\lambda(z)$ is the canyon unit width, depending on z. The standard deviation between numerical and experimental profiles, averaged among all the simulations, was found to be 0.02 for the first order statistics, 0.12 for the second order statistics and 0.26 for the third order statistics. It is worthwhile noting that closer to the canyon up to $z/H = 3$, the statistics profiles of numerical (solid lines) and experimental (dashed lines) skewness profiles display a better match (Fig. 2). A higher variability observed from $z/H = 3$ level up to the top could be blamed on one hand to the occurrence of large turbulent structures, which need a very large sample dataset to be completely resolved (Rossi and Iaccarino, 2013), and on the other hand to limitations in the upper part of the experimentally simulated boundary layer: a higher degree of uncertainty of the experimental acquisition for the highest velocity flow particles as well as the influence of the water-air interface (Garau et al., 2018). The mean stream-wise velocities made non-dimensional by the free-stream velocity, U_{ref}, at $z/H = 7$ (where $z/H = 7$ is the maximum height available for experimental simulations), match very well especially inside the canyon. Some small differences are visible just above the building top in case of flat roofs for both $AR_C = 1$ and 2 (blue lines in panels a, c), and between $2 < z/H < 4$, in case of square section canyon with 45° sloped roof (green lines in panel a).

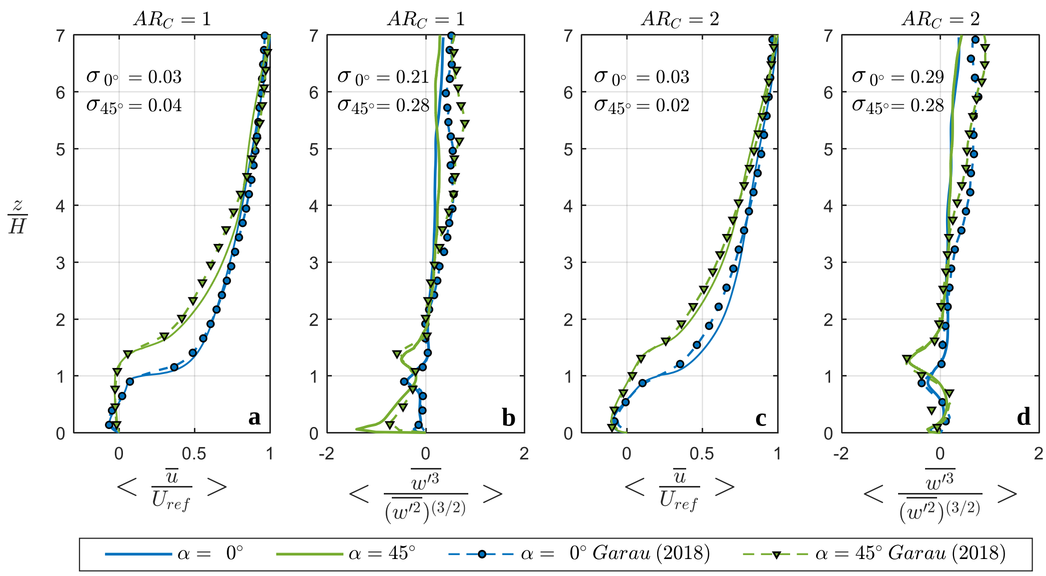

Fig. 1: Comparisons between numerical (solid line) and laboratory (dashed line with symbols) experiments. The horizontally averaged profiles of the mean stream-wise velocity made non dimensional by the free-stream velocity, U_{ref} (a, c) and the mean skewness of the vertical velocity profiles (b, d), (computed $z/H = 7$).

As for the skewness factor (Fig. 2 b, d), the highest differences are visible above $z/H = 3.5$, where for all the cases, the laboratory data appear to grow faster than the numerical ones, whereas above $z/H = 6$ they converge towards the numerical curves. The mean standard deviation between numerical and experimental profiles in these four configurations was found equal to 0.26 when computed on all the profiles up to $7H$, but equal to 0.10 if only the lowest part, up to $3.5H$, is taken into account. In the lowest region, below the $z/H = 3.5$ level, the configuration that more deviates from experimental results is AR_C =1, $\alpha = 45°$, showing some discrepancies in values but not in the overall behaviour, near the bottom (Fig. 3a).

In order to compare the spatial patterns, Fig. 3 and Fig. 4 show the streamlines of the mean velocity field superimposed to the vertical velocity skewness colour maps in the four cases used for validation. The streamlines exhibit the typical features of the skimming flow regime (panels b, c, e and f in Fig. 3) and wake interference (panels b, c, e and f in Fig. 4), which are common also for the other roof slopes. According to Oke, (1988), the skimming flow regime is valid for $AR_C < 1.5$, while the wake interference regime corresponds to $1.5 < AR_C < 3.5$. For the skimming flow regime (Fig. 3), a main stable vortex occupies the entire canyon, with two small counter-rotating vortexes sit in the corners between the bottom and the building façades, which become very small with increasing roof pitch (panels e and d in Fig. 3). In the case of wake interference (Fig.4) there are "secondary flows in the canyon space where the downward flow of the cavity eddy is reinforced by deflection down the windward face of the next building downstream" (Oke, 1988): two counter rotating vortexes are apparent for flat buildings (panels b and c in Fig. 4) while the upwind vortex almost vanish for $\alpha = 45°$. Indeed, as already pointed out by Badas et al. (2017) and Garau et al. (2018) the flow topology and the transition limits among the flow regimes, traditionally studied with reference to flat roof buildings, are affected by presence of gable roof.

The comparison of numerical (panels b and e) and laboratory (panels c and f) skewness fields together with the corresponding mean vertical profiles is shown in Fig. 3 and 4: the map fields present the same crucial elements and despite some differences are foreseen, both vertical profile and spatial patterns are in good agreement and allow having an adequate confidence in numerical data. Both the datasets show, for the two investigated aspect ratios, a negative skewness value tongue going from the upwind pitch to the downwind building eaves, and then protruding towards the canyon bottom. The transition lines between negative and positive regions (black continuous lines) demonstrate also a good agreement between numerical and experimental results, although the latter are slightly noisier.

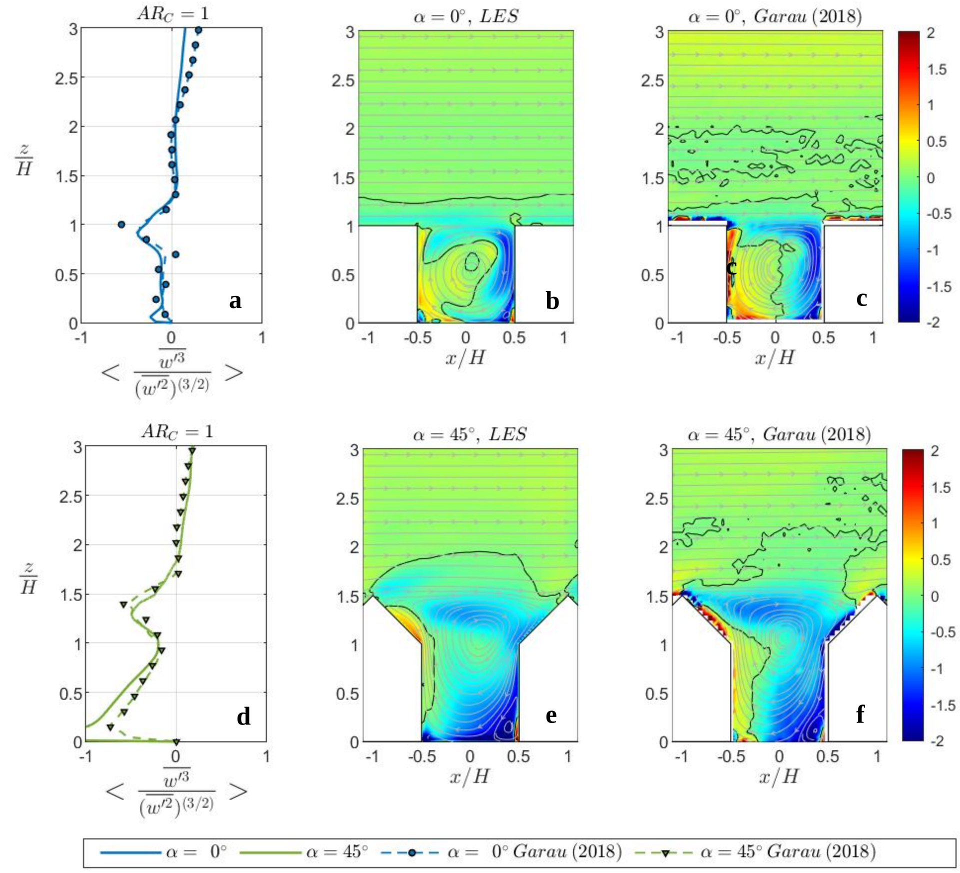

Fig. 2: Horizontally averaged profiles (a, d) and maps for numerical (b, e) and laboratory (c, f) experiments of the mean skewness of the vertical velocity profiles. All data are made non dimensional by the free-stream velocity, U_{ref}. Comparisons are plotted for $AR_C = 1$ and flat roof (first row panels) or $\alpha =$ 45° (second row panels), up to $z/H = 3$. The black lines indicate the zero crossing.

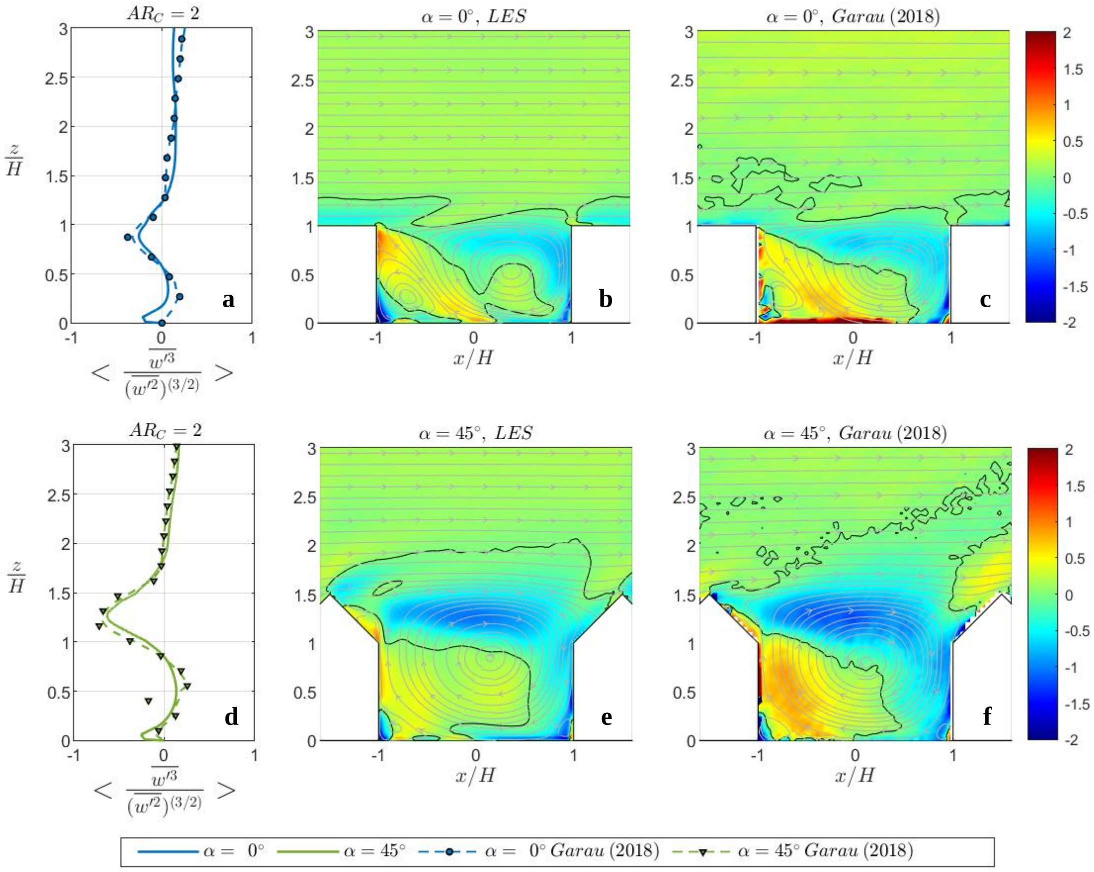

Fig. 3: Horizontally averaged profiles (a, d) and maps for numerical (b, e) and laboratory (c, f) experiments of the mean skewness of the vertical velocity profiles. All data are made non dimensional by the free-stream velocity, U_{ref}. Comparisons are plotted for $AR_C = 2$ and flat roof (first row panels) or α = 45° (second row panels), up to $z/H = 3$. The black contour lines indicate the zero crossing.

3 Results

The Quadrant Analysis (QA) was here employed to assess how the presence of gable roof and its slope affects the Reynolds stress contributing terms. The theoretical framework is briefly drawn in the following, while for an in-depth review of QA the reader is referred to Wallace (2016). In order to separate different vertical, turbulent momentum flux ($\overline{u'w'}$) contributions, Wallace et al. (1972), who first introduced the QA, split the Cartesian $u' - w'$ plane into four quadrants (see Fig. 10a), according to the sign of the fluctuating velocity components: $Q_1(u' > 0,\ w' > 0)$, $Q_2\ (u' < 0,\ w' > 0)$, $Q_3(u' < 0,\ w' < 0)$ and $Q_4(u' > 0,\ w' < 0)$, and the turbulent momentum flux is then separately computed in each quadrant. In the following, the term $\overline{u'w'}_i$ represents the turbulent momentum contribution corresponding to the quadrant Q_i and contributions are made non dimensional by U_{ref}.

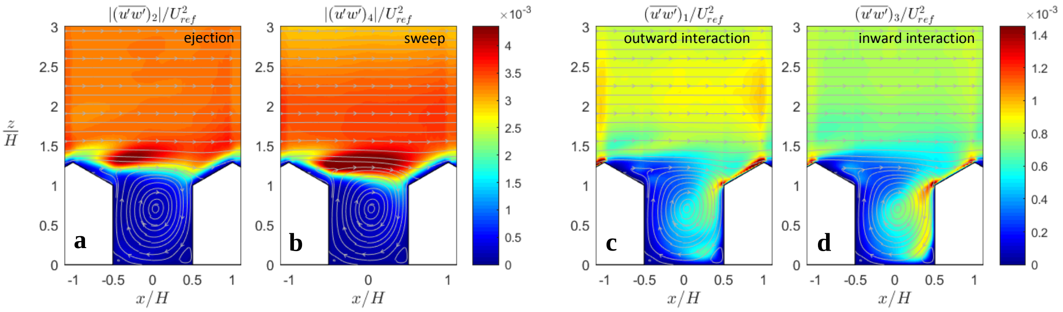

Fig. 4: Quadrant analysis of the vertical momentum flux fields $|\overline{u'w'}|/U^2{}_{ref}$ for the configuration $AR_C = 1$, α = 30°: the spatial maps represent the absolute values of the relative magnitudes for ejections (Q_2, panel a), sweeps (Q_4, panel b), outward interactions (Q_1, panel c), inward interactions (Q_3, panel d), and the superimposed streamlines of the mean velocity magnitude. Two different colour-bars are employed for even (a, b) and odd (c, d) quadrants.

As an example, Fig. 5 displays the maps of the absolute value of the contribution to the turbulent momentum flux from the four quadrants in the case of $AR_C = 1$ and $\alpha = 30°$. The Q_2 and Q_4 quadrants correspond respectively to ejection, or burst-like events (i.e. low momentum fluid transported upwards – Fig. 5a), and sweep events (i.e. high momentum fluid transported downwards – Fig. 5b): they are gradient-wise motions and represent organized events, normally giving the largest contributions to the momentum flux for wall bounded flows (Raupach, 1981), as occurring in the present case. The Q_2 (ejection – Fig. 5a) and Q_4 (sweep – Fig. 5b) colour maps show similar patterns, with a sharp distinction between low and quite uniform values inside the canyon and higher values just above the eaves, at the interface between the canyon and the external flow. The Q_1 (Fig. 5c) and Q_3 (Fig. 5d) motions are named outward and inward interactions: they are counter-gradient-wise motions, represent the unorganized part of the flow, and they generally give a minor contribution to the momentum flux. Indeed, Fig. 5 displays two colour-bars, and the one used for the even quadrants has a range extent three times larger than the colour scale of the odd quadrant maps.

Moreover, in this specific case, as well as for the other investigated conditions, Q_1 (outward interaction) and Q_3 (inward interaction) show higher values in the flow overlaying the canopy, similarly to Q_2 and Q_4. However, high values of the odd contributions propagate within the canyon, differently from what observed for the even quadrants. Specifically, Q_1 and Q_3 are very low in the lee of the upwind building (including the roof), whereas in the proximity of the windward roof and façade of the downwind building a layer of high values is apparent. The strength and penetration inside the canyon of that region, and specifically the downward momentum transport (depending on inward interaction - Q_3), are closely related to both the roof slope and the canyon aspect ratio. Since sweeps (Q_4) appear to give the most important contribution to momentum flux in the shear layer, where the exchange between canyon and surrounding air takes place, the sweep colour maps for three of the simulated roof slopes ($0°, 20°, 45°$) and the two AR_C are plotted in Fig. 6 and 7 (respectively for $AR_C = 1$ and 2) to show the dependence on the slope and canyon aspect ratio. Sweep contribution (Q_4) remains homogeneously low inside the canyon, whereas the highest contributions are found within the shear layer developing between the eave and the roof top. A comparative analysis of the maps of Fig. 6 and Fig. 7 shows that the thickness of the shear layer depends on the roof slope and is a minimum for the flat roof case (Fig. 6a). Within and above the shear layer, the Q_4 contribution to the turbulent momentum flux increases with roof slope, particularly in the case of skimming flow (Fig. 6) but also in case of wake interference regime (Fig. 7).

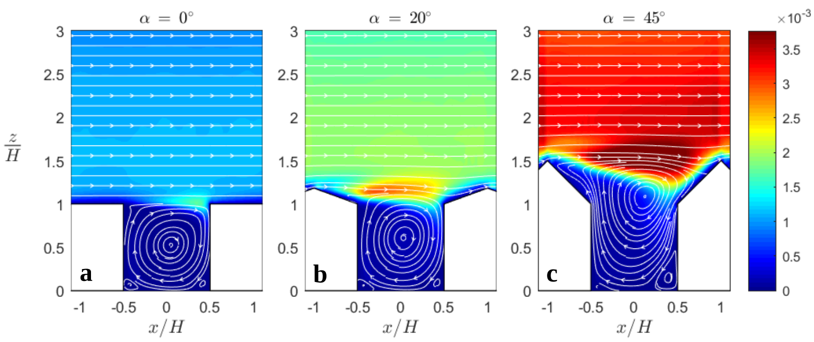

Fig. 5: Absolute values of the sweeps, $|Q_4|/U^2_{ref} = |(\overline{u'w'}_4)|/U^2_{ref}$, for configurations with $AR_C = 1$, and α = 0° (a), α = 20°(b) and α = 45° (c). Streamlines of the mean velocity field are superimposed (white lines).

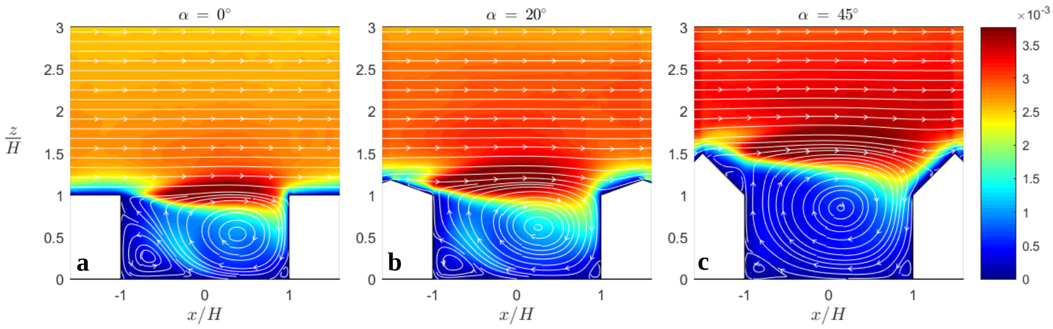

Fig. 6: Absolute values of the sweeps, $|Q_4|/U^2{}_{ref} = |(\overline{u'w'}_4)|/U^2{}_{ref}$, for configurations with $AR_C = 2$, and $\alpha = 0°$ (a), $\alpha = 20°$ (b) and $\alpha = 45°$ (c). Streamlines of the mean velocity field are superimposed (white lines).

In the wake interference regime ($AR_C = 2$), relatively high Q_4 values are present within the canyon also in between the two counter rotating vortexes (Fig. 7 a, b) while, above the eaves, a layer of high Q_4 values whose vertical extension increases from α = 0° (a) to α = 45° one (c) is apparent.

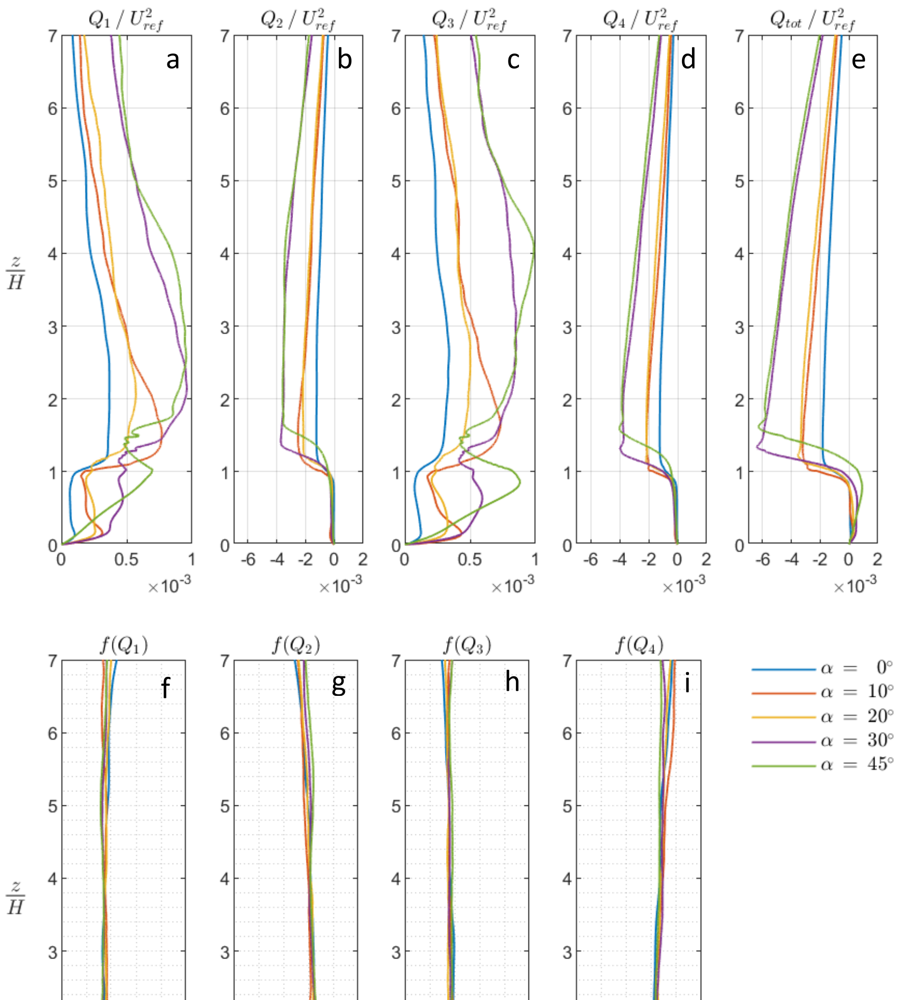

Fig. 7: Vertical momentum transfer made non-dimensional by the reference velocity for $AR_C = 1$. Upper row: horizontally averaged profiles of the four quadrant contributions (panels a−d) and total vertical momentum transfer (panel e). Lower row: frequency of the four contributions at the different pitch angles (panels f−i).

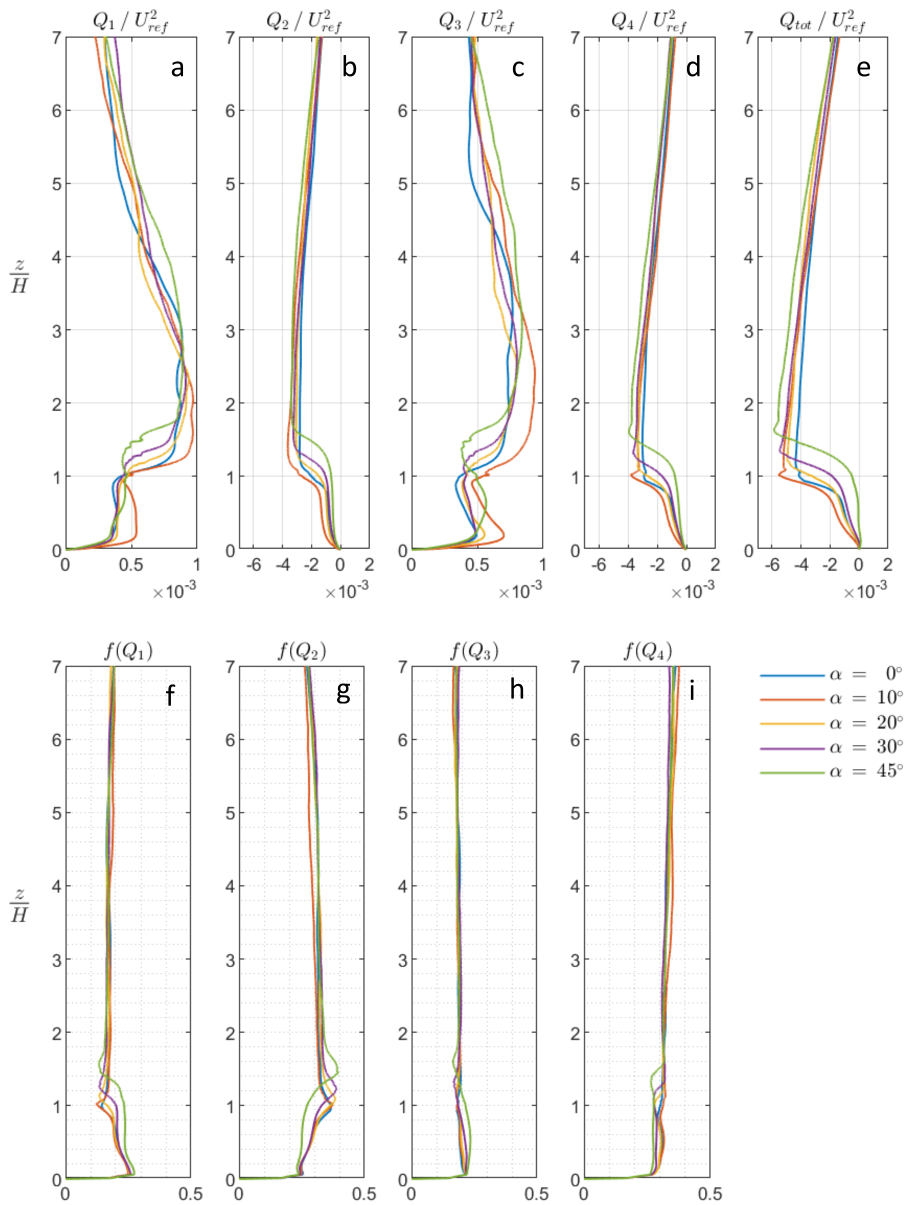

Fig. 9: Vertical momentum transfer made non-dimensional by the reference velocity for AR_C = 2. Upper row: horizontally averaged profiles of the four quadrant contributions (panels a–d) and total vertical momentum transfer (panel e). Lower row: frequency of the four contributions at the different pitch angles (panels f–i).

Other than QA spatial maps, we investigated the vertical profiles of quadrant contribution to the turbulent momentum flux, as well as their corresponding frequencies, which are both spatially averaged over the canyon unit (see Eq. 6). Results are plotted for all the slopes of the investigated range (0° − 45°) and the two canyon aspect ratios $AR_C = 1$ and

$AR_C = 2$ in Fig. 8 and Fig. 9, respectively. The presence of the pitched roof causes a general increase of the momentum transfer in the roughness sublayer (Fig. 8e and 9e). The total turbulent momentum flux increases for gable roofs, especially for $AR_C = 1$, but the four quadrants do not contribute to this increment in the same proportion: the relative importance of sweeps (Q_4, Fig. 8b) and ejections (Q_2, Fig. 8d) becomes more prominent for increasing roof slope. In accordance to Cheng and Liu (2011), sweeps (Q_4) and ejections (Q_2) prevail in the shear layer, both in terms of their contribution (as also apparent in Fig. 5) and occurrence frequency. Thus, their contribution basically drives the overall momentum transfer behaviour. Q_4 (sweeps) exhibits a peak at the rooftop height, irrespective of the pitch angle, as seen also in Fig. 6 and 7 despite Q_2 having a higher occurrence frequency at the same height. Q_2 (ejections) is a (smoother) maximum just above rooftop height. In summary, we observe that the behaviour of the even quadrant contributions is affected by the roof pitch in two ways: i.e. by changing the maximum value and changing the height where the maximum is located. The combined effect justifies the fact that, at the eaves' height, the Q_2 and Q_4 contributions can be lower for 45° pitched roof compared to lower angle configurations. With $AR_C = 1$, the increase in the magnitude of the momentum transfer seems to have a step behaviour: lower values for flat roof; then similar, a little higher, values for $\alpha = 10°$ and $\alpha = 20°$, and finally similar, highest values for $\alpha = 30°$ and $\alpha = 45°$. A similar step behaviour is not apparent for $AR_C = 2$. Above the rooftop, Q_2 and Q_4 display linearly decreasing contributes, while around the top of the investigated domain ($z = 7H$) Q_2 prevails in all the analysed simulations, although corresponding to lower frequencies than Q_4 ones. Inside the canyon, the role of outward (Q_1) and inward (Q_3) contributions becomes more important, and in case of 45° roof slope, $AR_C = 1$, they dominate both the frequency and the Reynolds stress contribution, due to the momentum transfer occurring near the windward wall.

In order to unveil how "the larger, energetic motions which occur relatively seldom are the principal source of Reynolds stress" (Wallace and Brodkey, 1977), and to single out the contribution of intense Reynolds shear stress events within each quadrant, the so-called "hole analysis" is often applied in different contexts, from turbulent boundary layers (Willmarth and Lu 1972; Lu and Willmarth 1973), flow over wall roughness (Raupach, 1981) and vegetated canopies (Poggi et al., 2004; Yue et al., 2007), to grid turbulence (Raushan et al., 2018). A hyperbolic threshold H_s is used to define the "hole" and contributions outside that region, i.e.:

$$|u' w'| \geq H_s |(\overline{u' w'})|, \qquad (7)$$

are considered when computing corresponding statistics (see Fig. 10a).

Fig. 10b presents the hole analysis performed on the canyon periodic unit for the case $AR_C = 1$ and flat buildings. Solid color lines represent the quadrant fractional contributions to the turbulent momentum flux lying outside the hole (Eq. 7), versus the hole size, H_s; the plot also shows the contribution from all the quadrants from events lying within the hole (solid black line) and the percentage of time spent within the hole (dashed blue line). The plot is remarkably in agreement with the results obtained by (Willmarth and Lu 1972), who performed the hole analysis at a specific non-dimensional distance from the wall in case of a turbulent boundary layer. Namely, for all the H_s the contributions from ejections (Q_2) and sweeps (Q_4) are larger than those from outward (Q_1) and inward (Q_3) interactions, and above the threshold $H_s = 6$, ejections (Q_2) and sweeps (Q_4) almost represent the whole contribution to the vertical turbulent momentum flux. However, although Q_2 being higher than Q_4, their difference is less marked with respect to the aforementioned results, due to the different nature of the two flows. Comparing the total contribution (black solid line) and the corresponding time spent within the hole (dotted blue line), it is apparent how, despite a large fraction of the time is spent within the hole for high H_s values, there are short periods of intense activity that bring to a non-negligible turbulent momentum flux contribution (for instance, the contribution for $H_s > 10$ is roughly the 10% of the total, despite corresponding to occurrence time less than 5%). For the other investigated cases, the results are very similar to Fig. 10b, since, when averaged on the whole vertical extension, they all represent the overall contribution of a boundary layer over a rough terrain, hence they have very similar behaviour.

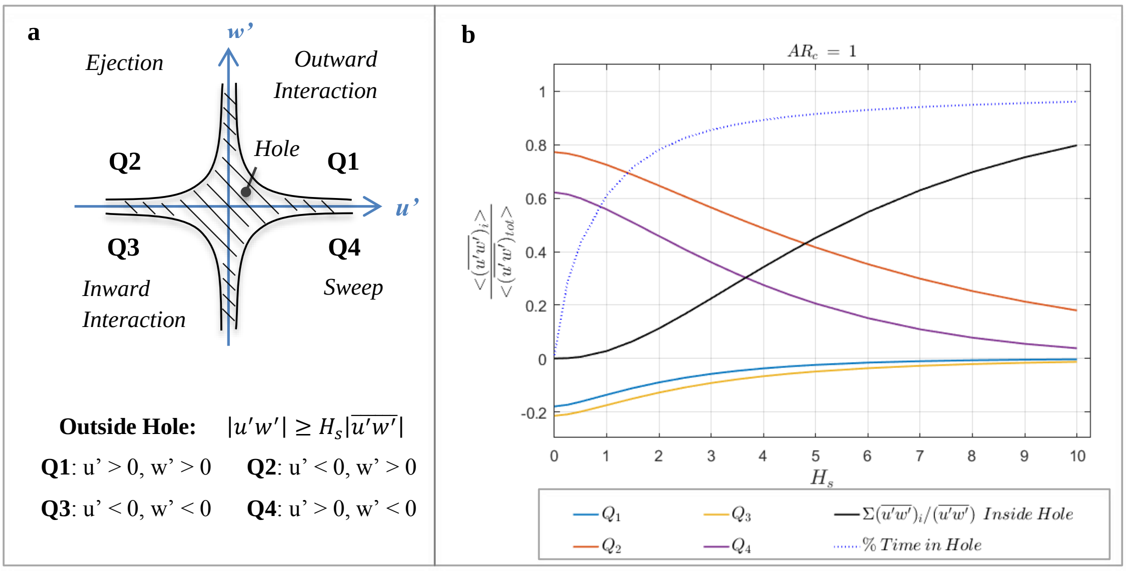

Fig. 10: (a): Sketch of the hole quadrant analysis (Willmarth and Lu, 1972); (b): hole analysis performed on the overall canyon unity for flat buildings and unity canyon aspect ratio: quadrant contributions to the turbulent momentum flux outside the hole, vs the hole magnitude H_s for Q_1(blue solid line); Q_2 (red solid line) Q_3 (yellow solid line); Q_4 (violet solid line); contribution of all quadrants inside the hole (black solid line); percentage of time spent within the hole (blue dashed line).

The influence of the roof slope and canyon aspect ratio is investigated by applying the hole analysis at the roof top height, since it represents the separation between the canyon and the external flow and corresponds to a characteristic region in QA spatial patterns and profiles (Fig. 5-9). Results for all the analyzed slopes are displayed in Fig. 11 (panels a and b present the results obtained for $AR_C = 1$ and 2, respectively).

For all the examined configurations, the predominance of ejections (Q_2) and sweeps (Q_4) with respect to outward (Q_1) and inward (Q_3) contribution is confirmed. Nonetheless, an inversion between Q_2 and Q_4 contributions is observed: differently from Fig. 10, Fig. 11 shows higher values for sweeps (Q_4) compared to ejections (Q_2). Moreover, for the threshold, H_s, higher than 6, Q_2 values are very low, and for gable roofs data collapse on a single line already for $H_s > 4$ in the case of $AR_C = 1$, while Q_4 represents almost the only remaining contribution to the turbulent momentum flux. The shift between Q_2 and Q_4 trends from Fig. 10 to Fig. 11 is due to the difference in considering the effect of a boundary layer as a whole (as done in Fig. 10, by averaging the contribution over the canyon unit) with respect to focusing on the mixing layer (as in Fig. 11, which displays the analysis at the roof top).

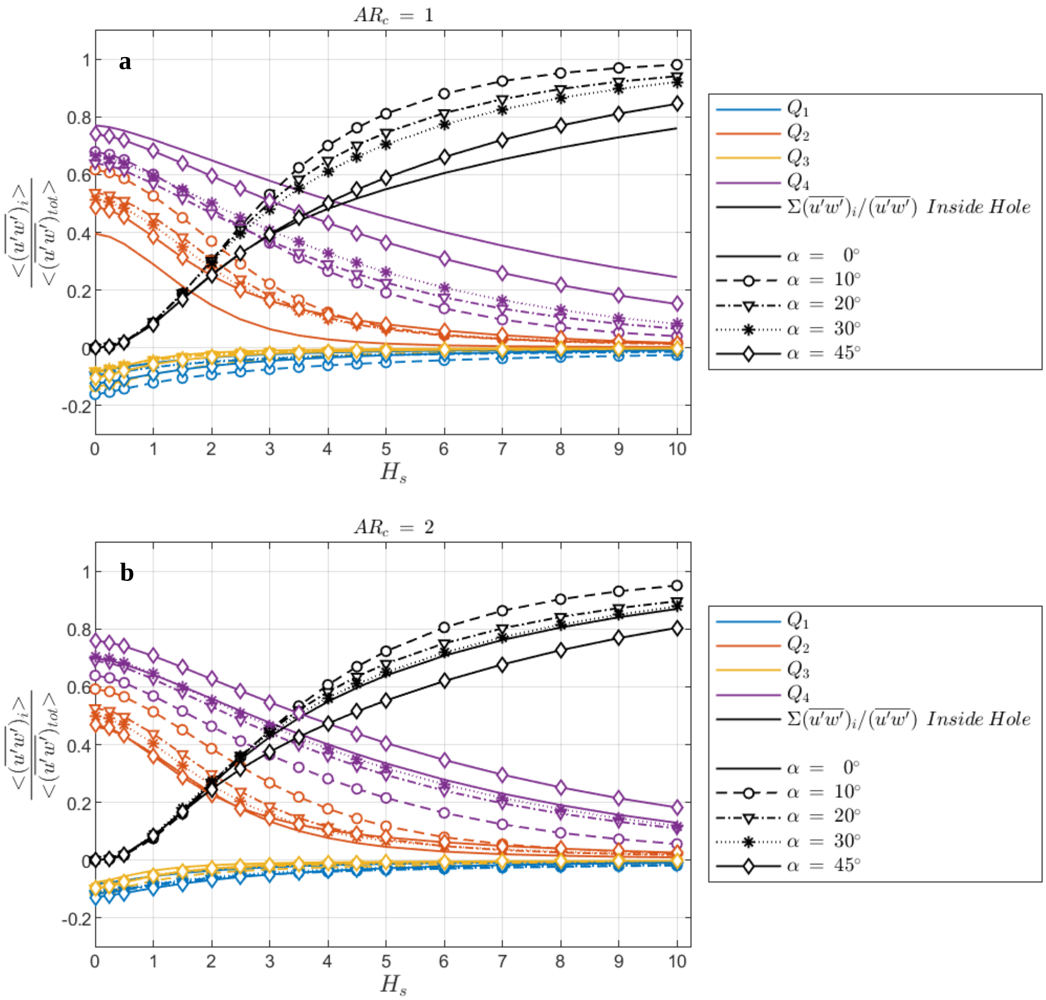

Fig. 8: Hole analysis of the quadrant contributions to the turbulent momentum flux outside the hole, vs the hole magnitude H_s; contributions are spatially averaged at the roof level, for $AR_C = 1$ (a), $AR_C = 2$ (b) and different roof slopes (simple line for 0°; circle for 10°; triangle for 20°; star for 30°; diamond for 45°). Q_1: blue, Q_2: red, Q_3: yellow, Q_4: violet, contribution of all quadrant inside the hole: black.

Moreover, a trend emerges in Fig. 11: the higher the roof pitch, the higher the sweep contribution (Q_4) and, correspondingly, the lower the ejection one (Q_2). This trend arises for both the canyon aspect ratios, but the effect is more apparent for $AR_C = 1$ (Fig. 11a). The flat roof case deviates from this general trend, being closer to the 45° roof slope than to the 10° case for both the canyon aspect ratios. In all the analysed cases, the quadrant contributions change with H_s following quite similar trends but, for high H_s values, the remaining Q_4 contribution is rather different. For instance, Fig. 11a shows that when $H_s = 10$ in the case of flat roof, sweep contribution, Q_4, still accounts for the roughly 10% of the total momentum flux, and the same value holds true for $\alpha = 45°$ while this value decreases monotonically for gable roofs, becoming negligible in case of $\alpha = 10°$.

Fig. 12 shows the excess of sweeps contribution with respect to ejections, relative to the total momentum transfer, $\left(< \overline{u'w'}_4 > - < \overline{u'w'}_2 >\right) / < \overline{u'w'}_{tot} >$, in the framework of the hole analysis. As commented for Fig. 11, there is an increase of the relative contribution for increasing roof slopes for both the canyon aspect ratios. However, the flat roof case deviates from this trend and corresponds to the highest curve in case of the $AR_C = 1$, while being the second highest curve in case of $AR_C = 2$. In addition, all the lines show a relative maximum, highlighted with a red dot in Fig. 12, whose position is displaced towards higher H_s values with decreasing roof slope, except for the flat roof case.

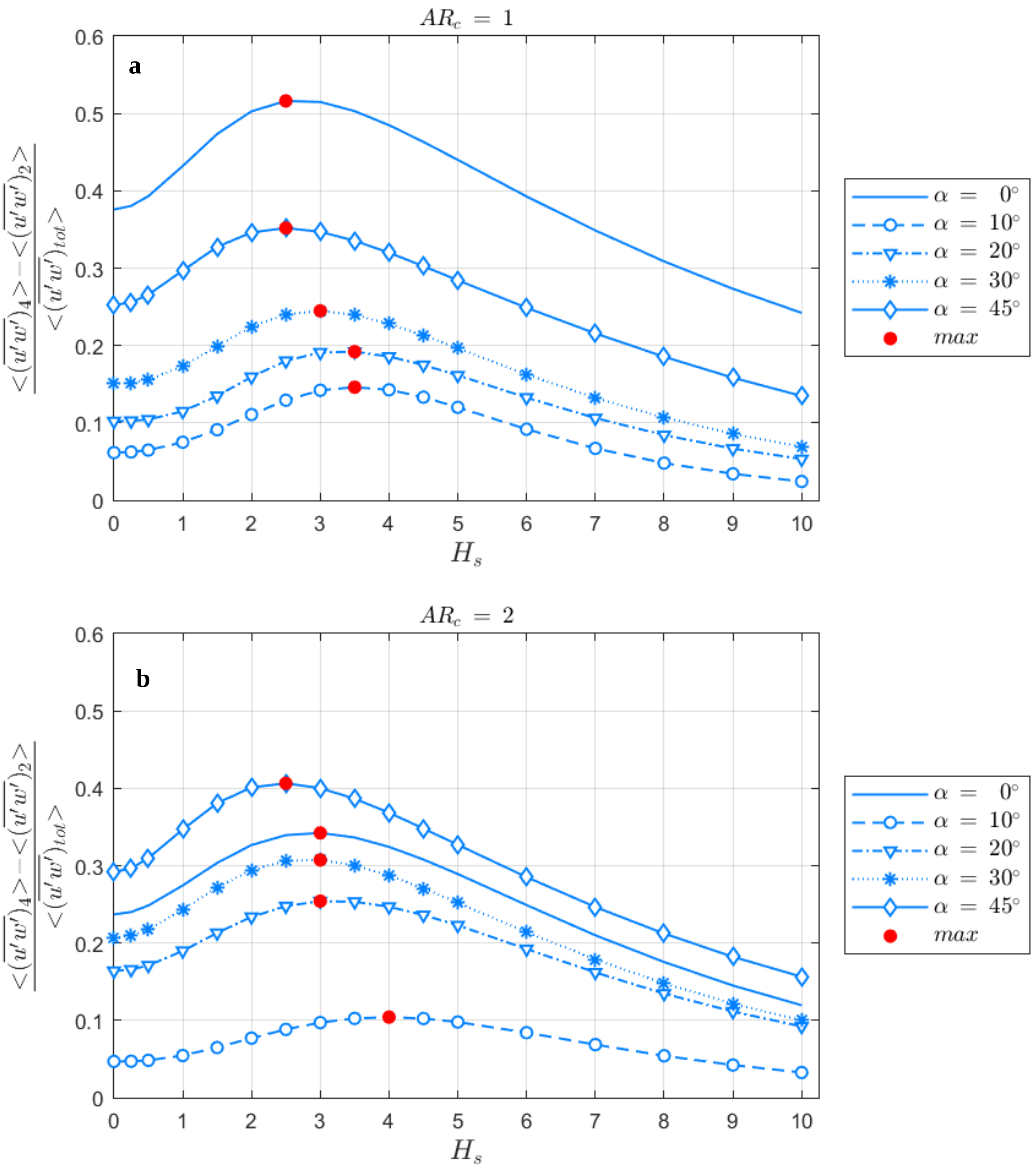

Fig. 9: Hole analysis of the relative contribution, $(Q_4 - Q_2)/ < \overline{u'w'}_{tot} >$, computed outside the hole, and spatially averaged at the rooftop level, vs the hole magnitude H_s, for $AR_C = 1$ (a), $AR_C = 2$ (b) and different roof slopes (plain line for 0°; circle for 10°; triangle for 20°; star for 30°; diamond for 45°). Red dots indicate the maximum values along each line.

Fig. 13 displays the vertical profile of Q_4/Q_2 ratio obtained by considering all the events (i.e. $H_s = 0$) for all the roof slopes (represented by different colours) and the two canyon aspect ratios ($AR_C = 1$ and $AR_C = 2$, plotted with solid and dashed lines respectively). Here, the height is made non-dimensional by the rooftop height, H_{tot}. All the cases converge towards the predominance of ejections ($Q_4/Q_2 < 1$) for high z/H_{tot}, i.e. the typical behaviour of a boundary layer far enough from the rough wall. Irrespective of the canyon aspect ratio, and for all the roof slopes, near the rooftop (close to $z/H_{tot} = 1$) there is a sharp peak corresponding to ratios higher than one, highlighting the dominance of sweeps (Q_4) in the interfacial shear layer.

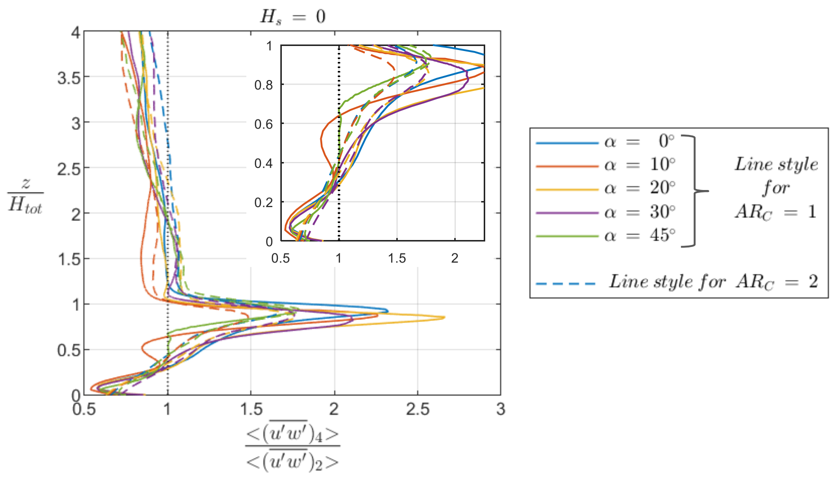

Fig. 13 Horizontally averaged profile of the mean Q_4/Q_2 ratio for the ten configurations, as in the legend: solid lines for $AR_C = 1$; dashed lines for $AR_C = 2$, and different roof slopes indicated by different colours. Data are made non dimensional with the total height of buildings (H_{tot}) both in the main panel and in the inset. The black dashed line corresponds to $Q_4/Q_2 = 1$.

Deeper inside the canyon, the ratio of sweeps (Q_4) to ejections (Q_2) decreases, till ejections start prevailing again in the bottom part of the canyon ($z/H_{tot} < 0.4$): in the case of higher aspect ratio, $AR_C = 2$ (see also the dashed lines in the inset of Fig. 13), this trend is monotonic while in the case of $AR_C = 1$ there is still an ejection predominance, but all the lines present a minimum value near $z/H_{tot} = 0.1$. Hence, the canopy layer is dominated by the sweep quadrant whilst in the above inertial sublayer ejections lead.

This behaviour is quite different from the one observed by Poggi et al., (2004) in the case of forest canopy, where the Q_4/Q_2 ratio has a quite constant trend inside the canopy (characterized by weak ejections in sparse canopies and by strong sweeps within dense canopies) probably also due to the three-dimensionality of the obstacles of the vegetated canopy.

In order to assess the effects on the momentum transport efficiency and identify any trend related to the roof slope variability, the correlation coefficient was computed:

$$r_{uw} = \langle \frac{\overline{u'w'}}{\sqrt{\overline{u'^2}}\sqrt{\overline{w'^2}}} \rangle \quad (8)$$

Fig. 14 displays the vertical profile of the correlation coefficient horizontally averaged over the roughness periodic unit, r_{uw}; vertical coordinates are made non-dimensional by the eaves' height, H. All the curves present a minimum value around -0.5 near the rooftop level (as highlighted in the inset of Fig. 14, where data are plotted versus z/H_{tot}). This is the same value (-0.5) obtained for neutrally stratified roughness sublayer and for vegetated canopies (Finnigan, 2000), while the above region displays lower absolute values, which is a sign of a more efficient momentum transfer of the urban canopy with respect to the above layers. At higher elevations above the canopy, r_{uw} is roughly constant around -0.4 for all the analysed cases, while for elevations larger than 6 H, all curves show an increasing trend and they approach towards slightly higher values than -0.32, i.e. the standard inertial sublayer value in case of a constant stress surface layer (Garratt, 1994).

Inside the canopy, the profiles are mainly dependent on AR_C: when $AR_C = 1$, r_{uw} trends have positive values except near the cavity top, whilst for $AR_C = 2$, r_{uw} follows the same monotonic trend toward the axis origin for all cases, except for 45° roof slope, collapsing on a single line. This trend resembles the family portrait of forest canopies identified by Böhm et al., (2013) and Raupach et al., (1996). Instead, in the case of $AR_C = 1$, the correlation coefficient inside the canyon is positive irrespective of the roof slope due to the prevalence of positive quadrant contribution (inward and outward interaction) with respect to the negative ones (sweep and ejections), in agreement with what already observed in Fig. 8 and 9. Moreover, although a sharp trend with roof slope is not apparent, the higher r_{uw} absolute values at the roof height are found for the higher roof angles, pointing out a more efficient vertical momentum transfer.

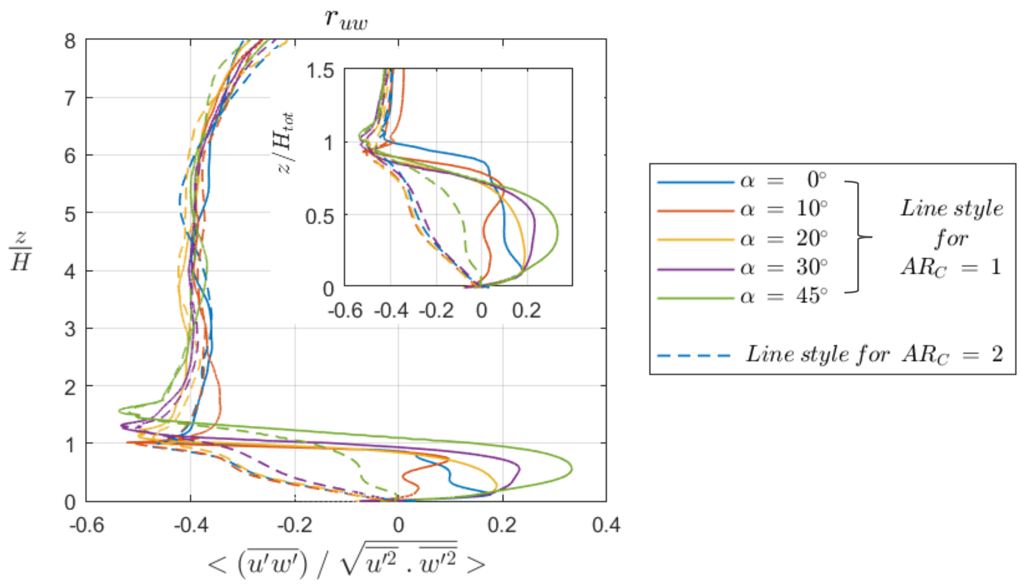

Fig. 10: Correlation profile, r_{uw}, for the ten configurations: solid lines for $AR_C = 1$; dashed lines for $AR_C = 2$. Different colours indicate different roof slopes as displayed in the legend. Data are made non dimensional respectfully using the eaves height (H), in the main plot, and total height is employed (H_{tot}) in the small inset.

4 Discussion

The QA analysis highlighted a different behaviour among the considered cases that is related to the different development of the shear layer. In order to investigate its growth and evolution, the shear layer thickness was computed at the rooftop by means of the vorticity thickness, which is a measure of the maximum local shear (Brown and Roshko, 1974):

$$\delta_\omega = \frac{U_2 - U_1}{\partial U/\partial y|_{max}} \tag{9}$$

where the maximum is computed along each vertical profile, while U_2 and U_1, in the present study, are taken as U_{ref} and 0 respectively.

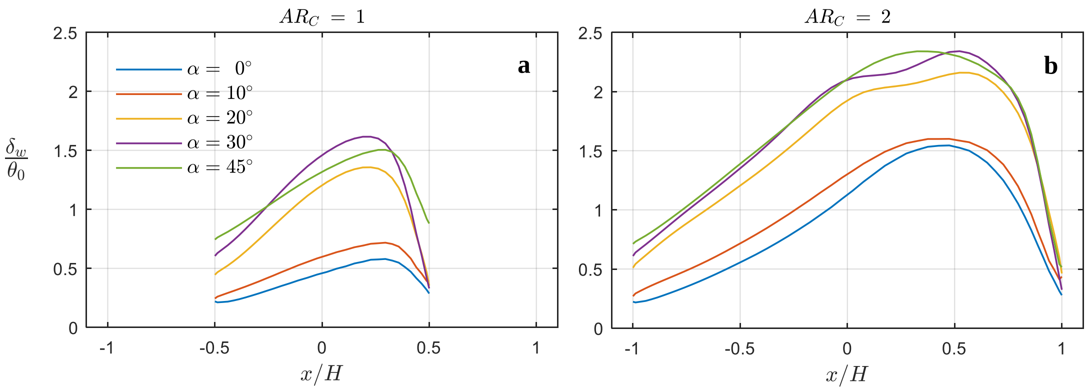

Fig. 11: Vorticity thickness δ_ω (Eq. 9) made non dimensional by the momentum thickness computed along a line at the rooftop level for the five roof slopes (with different colour as in the legend) and two aspect ratios (panel a for $AR_C = 1$; panel b for $AR_C = 2$).

Fig. 15 shows the variation of the vorticity thickness δ_ω along the cavity at the rooftop height, $\lambda(z = H_{tot})$, made non-dimensional by the momentum thickness θ_0 (which was computed from the velocity profiles at the upwind roof ridge in case of gable roof and at the leading edge for the flat roofs). The analysis is focused on the vorticity thickness evolution between the upstream and downstream corner of the cavity ($|x/H| <= AR_C/2$). The general trend displayed in Fig. 15 is similar to the ones reported in literature for cavity flows (Chang et al., 2006; Haigermoser et al., 2008; Kang et al., 2008). The vorticity thickness increases along the canyon cavity, it reaches a maximum close to the downwind building corner and then decreases. A trend with the roof slope is apparent. Indeed, the curves are shifted towards higher values when higher roof slopes are considered, and correspondingly their slope, hence the vorticity rate of growth, increases. This behaviour can be observed for both the aspect ratios, but it is more evident when $AR_C = 1$. A deviation from this behaviour is observed for the α = 45°, AR_C = 1 case, which displays lower values and slope compared to the α = 30° case.

For both the aspect ratios, two lines clusters emerge according to the roof slope, the first includes 0° and 10° whereas the second includes 20°, 30° and 45°. The latter issue is in contrast with the picture portrayed in Fig. 11, where a distinct trend between flat roof and gable roof was identified. Actually, this discrepancy confirms that the perspective deriving from mean flow analysis is very limited. Hence, for instance, turbulent closure development cannot rely on mean flow features (Krogstadt and Antonia, 1999). Here, a similar configuration confirmed by the smooth passage between the flow topology at increasing roof slope (Fig. 6-7) brings to similar vorticity thickness evolution for flat and $\alpha = 10°$ slope, despite the QA analysis identified a very different behaviour for flat roof buildings.

Variations of hole analysis have been proposed in literature, for instance Lu and Willmarth, (1973) defined the threshold on the product of stream-wise and vertical velocity standard deviations, while Narasimha et al., (2007) considered the Reynolds stress standard deviation. We however verified that, albeit obvious shift in the sample data, the obtained results are confirmed also using these hole definitions (for the sake of brevity, results are not presented here).

The analysis showed that presence of roofs does not alter the positive imbalance between sweeps (Q_4) and ejections (Q_2) (Fig. 11-13), a feature that is acknowledged to be universal for forest canopies, and it is synonymous of the mixing-layer mechanisms (Finnigan, 2000), but that does not hold true in other urban configurations, such as 3D diagonal array of cubes (Kanda, 2006). Nevertheless, the gable roof highly impacts on the relative importance of sweeps (Q_4) and ejections (Q_2) (Fig. 11 -13).

5 Conclusion

A LES simulation of periodic urban canopy was performed: two canyon aspect ratios were investigated, and roof pitch ranging from 0° to 45°. The systematic analysis presented above allows unveiling marked trends with increasing roof slope and, at the same time, a different behaviour of gable- with respect to flat-roof buildings in terms of decomposition of the Reynolds shear stress and on the intermittency of the momentum transfer. Quite a gradual variation with increasing slope is apparent for the mean velocity field and derived vorticity thickness, while a remarkable difference between flat and gable roof buildings emerged from quadrant analysis, in the repartition between ejection and sweep events and in their intermittency as identified by the hole analysis. The analysis of the present results suggests an explanation of the role of the gable roof in enhancing the momentum transfer. The vertical momentum flux is driven by the development of the interfacial shear layer at the canyon top. With flat roof, the Kelvin-Helmholtz instabilities characterising the shear layer begin developing at the upper, leeward, corner. Conversely, with gable roof, the development starts at the roof edge, i.e.

0.5 *H* upstream from leeward corner. The upstream shift of the initial shear layer developing point allows a longer length to the Kelvin-Helmholtz structures to grow and become unstable enhancing the mixing. This effect is more significant for AR_C = 1 because, for AR_C = 2, in the downstream portion of the interface, the shear layer is completely unstable and does not play a determinant role in the momentum exchange whatever the starting point. For α = 10° and α = 20°, however, the growth rate of the Kelvin-Helmholtz structures is limited by the small roof angle. Conversely, the effect is not present for the larger explored angles (α = 30° and α = 45°). Presumably, the limiting effect terminates at a critical angle in between 20° and 30°, but the present results do not allow a finer detection. Actually, the characterization of ejection (Q_2) and sweep (Q_4) events plays a key role in most of the structural models developed in the context of the wall-bounded turbulence to explain the redistribution of turbulent kinetic energy and momentum (Lozano-Durán et al., 2012), and it is also intimately linked to the evolution of coherent studies, which is presently under study.

Inherent limitations affect the present simulations, which are intentionally focused on idealized conditions, rather different from realistic conditions from many points of view. First of all, the analysis here presented refers to a periodic configuration of two-dimensional urban canyons, and the role of gable roof may have a different impact when different, more complex or heterogeneous urban texture is considered. Moreover, perpendicular incident wind and stationary conditions are simulated. Indeed, also in the case of stable stratification, small departure from the ideal stationary conditions, which are generally simulated in numerical and laboratory canyon models, as well as change in wind direction can have a determinant impact on the flow field in real conditions (Karra et al., 2017).

Nonetheless, the present work is a step forward to the characterization of the inner mechanisms of mixing above urban canyons, potentially useful for the development of parametrizations relevant in many contexts, from microscale to mesoscale models.

Acknowledgements This work was realized thanks to the collaboration with the CRS4 (Centre for advanced studies, research and development in Sardinia), which made its clusters available for numerical computation. This research has been partially funded by the Autonomous Region of Sardinia, FSC 2014-2020, Grant No. RASSR50082.

References

Air quality in Europe, 2018. European Environment Agency. https://www.eea.europa.eu/publications/air-quality-in-europe-2018 .

Badas, M.G., Ferrari, S., Garau, M., Querzoli, G., 2017. On the effect of gable roof on natural ventilation in two-dimensional urban canyons. Journal of Wind Engineering and Industrial Aerodynamics 162, 24–34. https://doi.org/10.1016/j.jweia.2017.01.006

Badas, M.G., Ferrari, S., Garau, M., Seoni, A., Querzoli, G., 2020. On the Flow Past an Array of Two-Dimensional Street Canyons Between Slender Buildings. Boundary-Layer Meteorol 174, 251–273. https://doi.org/10.1007/s10546-019-00484-x

Bazdidi-Tehrani, F., Kiamansouri, M., Jadidi, M., 2016. Inflow turbulence generation techniques for large eddy simulation of flow and dispersion around a model building in a turbulent atmospheric boundary layer. Journal of Building Performance Simulation 9, 680–698. https://doi.org/10.1080/19401493.2016.1196729

Besalduch, L.A., Badas, M.G., Ferrari, S., Querzoli, G., 2014. On the near field behavior of inclined negatively buoyant jets. EPJ Web of Conferences 67, 02007. https://doi.org/10.1051/epjconf/20146702007

Blocken, B., 2015. Computational Fluid Dynamics for urban physics: Importance, scales, possibilities, limitations and ten tips and tricks towards accurate and reliable simulations. Building and Environment, Fifty Year Anniversary for Building and Environment 91, 219–245. https://doi.org/10.1016/j.buildenv.2015.02.015

Böhm, M., Finnigan, J.J., Raupach, M.R., Hughes, D., 2013. Turbulence Structure Within and Above a Canopy of Bluff Elements. Boundary-Layer Meteorol 146, 393–419. https://doi.org/10.1007/s10546-012-9770-1

Brown, G.L., Roshko, A., 1974. On density effects and large structure in turbulent mixing layers. Journal of Fluid Mechanics 64, 775–816. https://doi.org/10.1017/S002211207400190X

Cai, X.-M., 2012. Effects of Wall Heating on Flow Characteristics in a Street Canyon. Boundary-Layer Meteorol 142, 443–467. https://doi.org/10.1007/s10546-011-9681-6

Chang, K., Constantinescu, G., Park, S.-O., 2006. Analysis of the flow and mass transfer processes for the incompressible flow past an open cavity with a laminar and a fully turbulent incoming boundary layer. Journal of Fluid Mechanics 561, 113. https://doi.org/10.1017/S0022112006000735

Chen, B., Cheng, H., Kong, H., Chen, X., Yang, Q., 2019. Interference effects on wind loads of gable-roof buildings with different roof slopes. Journal of Wind Engineering and Industrial Aerodynamics 189, 198–217. https://doi.org/10.1016/j.jweia.2019.03.033

Cheng, W.C., Liu, C.-H., 2011a. Large-eddy simulation of turbulent transports in urban street canyons in different thermal stabilities. Journal of Wind Engineering and Industrial Aerodynamics, The Fifth International Symposium on Computational Wind Engineering 99, 434–442. https://doi.org/10.1016/j.jweia.2010.12.009

Cheng, W.C., Liu, C.-H., 2011b. Large-Eddy Simulation of Flow and Pollutant Transports in and Above Two-Dimensional Idealized Street Canyons. Boundary-Layer Meteorol 139, 411–437. https://doi.org/10.1007/s10546-010-9584-y

Chung, T.N.H., Liu, C.-H., 2013. On the Mechanism of Air Pollutant Removal in Two-Dimensional Idealized Street Canyons: A Large-Eddy Simulation Approach. Boundary-Layer Meteorology 148, 241–253. https://doi.org/10.1007/s10546-013-9811-4

de Villiers, E., 2006. The Potential of Large Eddy Simulation for the Modeling of Wall Bounded Flows (PhD Thesis). Imperial College of Science, Technology and Medicine.

Di Bernardino, A., Monti, P., Leuzzi, G., Querzoli, G., 2015a. Water-Channel Study of Flow and Turbulence Past a Two-Dimensional Array of Obstacles. Boundary-Layer Meteorology 155, 73–85. https://doi.org/10.1007/s10546-014-9987-2

Di Bernardino, A.D., Monti, P., Leuzzi, G., Querzoli, G., 2015b. On the effect of the aspect ratio on flow and turbulence over a two-dimensional street canyon. International Journal of Environment and Pollution 58, 27–38. https://doi.org/10.1504/IJEP.2015.076581

Di Bernardino, A., Monti, P., Leuzzi, G., Querzoli, G., 2020. Turbulent Schmidt Number Measurements Over Three-Dimensional Cubic Arrays. Boundary-Layer Meteorol 174, 231–250. https://doi.org/10.1007/s10546-019-00482-z

Ferrari, S., Badas, M.G., Garau, M., Seoni, A., Querzoli, G., 2017. The air quality in narrow two-dimensional urban canyons with pitched and flat roof buildings. International Journal of Environment and Pollution 62, 347. https://doi.org/10.1504/IJEP.2017.089419

Finnigan, J., 2000. Turbulence in Plant Canopies. Annu. Rev. Fluid Mech. 32, 519–571. https://doi.org/10.1146/annurev.fluid.32.1.519

Franke, J., Hellsten, A., Schlunzen, K.H., Carissimo, B., 2011. The COST 732 Best Practice Guideline for CFD simulation of flows in the urban environment: a summary. International Journal of Environment and Pollution 44, 419–427. https://doi.org/10.1504/IJEP.2011.038443

Garau, M., Badas, M.G., Ferrari, S., Seoni, A., Querzoli, G., 2018. Turbulence and Air Exchange in a Two-Dimensional Urban Street Canyon Between Gable Roof Buildings. Boundary-Layer Meteorol 167, 123–143. https://doi.org/10.1007/s10546-017-0324-4

Garratt, J.R., 1994. Review: the atmospheric boundary layer. Earth Science Reviews 37, 89–134. https://doi.org/10.1016/0012-8252(94)90026-4

Gullbrekken, L., Uvsløkk, S., Kvande, T., Pettersson, K., Time, B., 2018. Wind pressure coefficients for roof ventilation purposes. Journal of Wind Engineering and Industrial Aerodynamics 175, 144–152. https://doi.org/10.1016/j.jweia.2018.01.026

Haigermoser, C., Vesely, L., Novara, M., Onorato, M., 2008. A time-resolved particle image velocimetry investigation of a cavity flow with a thick incoming turbulent boundary layer. Physics of Fluids 20, 105101. https://doi.org/10.1063/1.2990043

Hoydysh, W.G., Griffiths, R.A., Ogawa, Y., 1974. A scale model study of the dispersion of pollution in street canyon. APCA Paper, APCA Paper 74–157. https://doi.org/Presented at the 67th APCA Annual Meeting

Huang, Y., He, W., Kim, C.-N., 2015. Impacts of shape and height of upstream roof on airflow and pollutant dispersion inside an urban street canyon. Environmental Science and Pollution Research 22, 2117–2137. https://doi.org/10.1007/s11356-014-3422-6

Kanda, M., 2006. Large-Eddy Simulations on the Effects of Surface Geometry of Building Arrays on Turbulent Organized Structures. Boundary-Layer Meteorol 118, 151–168. https://doi.org/10.1007/s10546-005-5294-2

Kang, W., Lee, S.B., Sung, H.J., 2008. Self-sustained oscillations of turbulent flows over an open cavity. Exp Fluids 45, 693. https://doi.org/10.1007/s00348-008-0510-8

Karra, S., Malki-Epshtein, L., Neophytou, M.K.-A., 2017. Air flow and pollution in a real, heterogeneous urban street canyon: A field and laboratory study. Atmospheric Environment 165, 370–384. https://doi.org/10.1016/j.atmosenv.2017.06.035

Krogstadt, P.-Å., Antonia, R.A., 1999. Surface roughness effects in turbulent boundary layers. Experiments in Fluids 27,450–460 https://doi.org/10.1007/s003480050370

Liu, C.-H., Cheng, W.C., Leung, T.C.Y., Leung, D.Y.C., 2011. On the mechanism of air pollutant re-entrainment in two-dimensional idealized street canyons. Atmospheric Environment 45, 4763–4769. https://doi.org/10.1016/j.atmosenv.2010.03.015

Liu, C.-H., Wong, C.C.C., 2014. On the pollutant removal, dispersion, and entrainment over two-dimensional idealized street canyons. Atmospheric Research 135–136, 128–142. https://doi.org/10.1016/j.atmosres.2013.08.006

Llaguno-Munitxa, M., Bou-Zeid, E., Hultmark, M., 2017. The influence of building geometry on street canyon air flow: Validation of large eddy simulations against wind tunnel experiments. Journal of Wind Engineering and Industrial Aerodynamics 165, 115–130. https://doi.org/10.1016/j.jweia.2017.03.007

Lozano-Durán, A., Flores, O., Jiménez, J., 2012. The three-dimensional structure of momentum transfer in turbulent channels. J. Fluid Mech. 694, 100–130. https://doi.org/10.1017/jfm.2011.524

Lu, S.S., Willmarth, W.W., 1973. Measurements of the structure of the Reynolds stress in a turbulent boundary layer. Journal of Fluid Mechanics 60, 481–511. https://doi.org/10.1017/S0022112073000315

Martilli, A., Clappier, A., Rotach, M.W., 2002. An Urban Surface Exchange Parameterisation for Mesoscale Models. Boundary-Layer Meteorology 104, 261–304. https://doi.org/10.1023/A:1016099921195

Narasimha, R., Kumar, S.R., Prabhu, A., Kailas, S.V., 2007. Turbulent flux events in a nearly neutral atmospheric boundary layer. Philosophical Transactions of the Royal Society A: Mathematical, Physical and Engineering Sciences 365, 841–858. https://doi.org/10.1098/rsta.2006.1949

Oke, T.R., 1988. Street design and urban canopy layer climate. Energy and Buildings 11, 103–113. https://doi.org/10.1016/0378-7788(88)90026-6

OpenFOAM 2.3.0 https://openfoam.org/version/2-3-0/

Ozmen, Y., Baydar, E., van Beeck, J.P.A.J., 2016. Wind flow over the low-rise building models with gabled roofs having different pitch angles. Building and Environment 95, 63–74. https://doi.org/10.1016/j.buildenv.2015.09.014

Poggi, D., Porporato, A., Ridolfi, L., Albertson, J.D., Katul, G.G., 2004. The Effect of Vegetation Density on Canopy Sub-Layer Turbulence. Boundary-Layer

Meteorology 111, 565–587. https://doi.org/10.1023/B:BOUN.0000016576.05621.73

Rafailidis, S., 1997. Influence of Building Areal Density and Roof Shape on the Wind Characteristics Above a Town. Boundary-Layer Meteorology 85, 255–271. https://doi.org/10.1023/A:1000426316328

Raupach, M.R., 1981. Conditional statistics of Reynolds stress in rough-wall and smooth-wall turbulent boundary layers. Journal of Fluid Mechanics 108, 363–382. https://doi.org/10.1017/S0022112081002164

Raupach, M.R., Finnigan, J.J., Brunei, Y., 1996. Coherent eddies and turbulence in vegetation canopies: The mixing-layer analogy. Boundary-Layer Meteorol 78, 351–382. https://doi.org/10.1007/BF00120941

Raushan, P.K., Singh, S.K., Debnath, K., 2018. Grid generated turbulence under the rigid boundary influence. Journal of Wind Engineering and Industrial Aerodynamics 182, 252–261. https://doi.org/10.1016/j.jweia.2018.10.003

Rossi, R., Iaccarino, G., 2013. Numerical analysis and modeling of plume meandering in passive scalar dispersion downstream of a wall-mounted cube. International Journal of Heat and Fluid Flow 43, 137–148. https://doi.org/10.1016/j.ijheatfluidflow.2013.04.006

Salizzoni, P., Soulhac, L., Mejean, P., Perkins, R.J., 2008. Influence of a Two-scale Surface Roughness on a Neutral Turbulent Boundary Layer. Boundary-Layer Meteorology 127, 97–110. https://doi.org/10.1007/s10546-007-9256-8

Shao, S., Tian, Y., Yang, Q., Stathopoulos, T., 2019. Wind-induced cladding and structural loads on low-rise buildings with 4:12-sloped hip roofs. Journal of Wind Engineering and Industrial Aerodynamics 193, 103948. https://doi.org/10.1016/j.jweia.2019.103948

Smagorinsky, J., 1963. General circulation experiments with the primitive equations. Mon. Wea. Rev. 91, 99–164. https://doi.org/10.1175/1520-0493(1963)091<0099:GCEWTP>2.3.CO;2

Spalding, D.B., 1962. A new analytical expression for the drag of a flat plate valid for both the turbulent and laminar regimes. International Journal of Heat and Mass Transfer 5, 1133–1138. https://doi.org/10.1016/0017-9310(62)90189-8

Takano, Y., Moonen, P., 2013. On the influence of roof shape on flow and dispersion in an urban street canyon. Journal of Wind Engineering and Industrial Aerodynamics 123, 107–120. https://doi.org/10.1016/j.jweia.2013.10.006

Tominaga, Y., Akabayashi, S., Kitahara, T., Arinami, Y., 2015. Air flow around isolated gable-roof buildings with different roof pitches: Wind tunnel experiments and CFD simulations. Building and Environment 84, 204–213. https://doi.org/10.1016/j.buildenv.2014.11.012

Tominaga, Y., Mochida, A., Yoshie, R., Kataoka, H., Nozu, T., Yoshikawa, M., Shirasawa, T., 2008. AIJ guidelines for practical applications of CFD to pedestrian wind environment around buildings. Journal of Wind Engineering and Industrial Aerodynamics, 4th International Symposium on Computational Wind Engineering (CWE2006) 96, 1749–1761. https://doi.org/10.1016/j.jweia.2008.02.058

Wallace, J.M., 2016. Quadrant Analysis in Turbulence Research: History and Evolution. Annual Review of Fluid Mechanics 48, 131–158. https://doi.org/10.1146/annurev-fluid-122414-034550
Wallace, J.M., Brodkey, R.S., 1977. Reynolds stress and joint probability density distributions in the u- v plane of a turbulent channel flow. The Physics of Fluids 20, 351–355. https://doi.org/10.1063/1.861897
Wallace, J.M., Eckelmann, H., Brodkey, R.S., 1972. The wall region in turbulent shear flow. Journal of Fluid Mechanics 54, 39–48. https://doi.org/10.1017/S0022112072000515
WHO (Ed.), 2006. Air quality guidelines: global update 2005 ; particulate matter, ozone, nitrogen dioxide and sulfur dioxide. WHO Regional Office for Europe, Copenhagen.
Willmarth, W.W., Lu, S.S., 1972. Structure of the Reynolds stress near the wall. Journal of Fluid Mechanics 55, 65–92. https://doi.org/10.1017/S002211207200165X
Xing, F., Mohotti, D., Chauhan, K., 2018. Study on localised wind pressure development in gable roof buildings having different roof pitches with experiments, RANS and LES simulation models. Building and Environment 143, 240–257. https://doi.org/10.1016/j.buildenv.2018.07.026
Yassin, M.F., 2011. Impact of height and shape of building roof on air quality in urban street canyons. Atmospheric Environment 45, 5220–5229. https://doi.org/10.1016/j.atmosenv.2011.05.060
Yue, W., Meneveau, C., Parlange, M.B., Zhu, W., van Hout, R., Katz, J., 2007. A comparative quadrant analysis of turbulence in a plant canopy: QUADRANT ANALYSIS PLANT CANOPY. Water Resour. Res. 43. https://doi.org/10.1029/2006WR005583
Zajic, D., Fernando, H.J.S., Brown, M.J., Pardyjak, E.R., 2015. On flows in simulated urban canopies. Environmental Fluid Mechanics 15, 275–303. https://doi.org/10.1007/s10652-013-9311-6
Zajic, D., Fernando, H.J.S., Calhoun, R., Princevac, M., Brown, M.J., Pardyjak, E.R., 2011. Flow and Turbulence in an Urban Canyon. Journal of Applied Meteorology and Climatology 50, 203–223. https://doi.org/10.1175/2010JAMC2525.1